Journal of Zhejiang University-SCIENCE A (Applied Physics & Engineering) *2024 25(7):557-572*
www.jzus.zju.edu.cn; www.springer.com/journal/11582
E-mail: jzus_a@zju.edu.cn

Research Article
https://doi.org/10.1631/jzus.A2300384

Check for updates

Influence of the penetration of adjacent X-section cast-in-place concrete (XCC) pile on the existing XCC pile in sand

Peng ZHOU[1,2,3], Jianhui XU[1], Changjie XU[1], Guangwei CAO[4]✉, Jie CUI[2], Xuanming DING[3]

[1]*School of Civil Engineering and Architecture, State Key Laboratory of Performance Monitoring and Protecting of Rail Transit Infrastructure, East China Jiaotong University, Nanchang 330013, China*
[2]*Guangdong Key Laboratory of Earthquake Engineering and Application Technology, Earthquake Engineering Research & Test Center, Guangzhou University, Guangzhou 510006, China*
[3]*Key Laboratory of New Technology for the Construction of Cities in Mountain Areas, College of Civil Engineering, Chongqing University, Chongqing 400045, China*
[4]*Zijin School of Geology and Mining, Fuzhou University, Fuzhou 350116, China*

Abstract: A series of small-scale 1*g* X-section cast-in-place concrete (XCC) pile-penetration model tests were conducted to study the effects of soil density and pile geometry on the lateral responses of an existing pile and the variations in surrounding soil stress. The results showed that the bending patterns of existing XCC piles varied with penetration depth. The lateral response of the existing pile was sensitive to the change in relative density and pile geometry. For example, the bending moment of the existing pile increased along with these parameters. The development of the radial stress σ'_r/σ'_{v0} of the soil around an existing pile showed different trends at various depths during the penetration of the adjacent pile. Moreover, the change in radial stress during the penetration of the XCC pile did not exhibit the "h/R effect" that was observed in the free-field soil, due to the shielding effect of the existing piles. The peak value of radial stress $\sigma'_{r\_max}/\sigma'_{v0}$ decreased exponentially as the radial distance r/R increased. The attenuation of $\sigma'_{r\_max}/\sigma'_{v0}$ with r/R in the loose sand was faster than in the medium-dense or dense sands. The $\sigma'_{r\_max}/\sigma'_{v0}$ at the same soil location increased with the cross-section geometry parameter.

Key words: X-section cast-in-place concrete (XCC) pile; Test; Penetration; Sand; Lateral response; Radial stress

1 Introduction

There are many types of piles used in engineering, which can be classified into circular and special-shaped piles in terms of cross-section geometry. In recent years, special-shaped piles have received widespread attention because of their superior bearing and deformation performance. X-section cast-in-place concrete (XCC) pile is one type of such special-shaped cross-section pile developed to improve efficiency and save material, which has been widely adopted in foundation reinforcement projects, such as highway and railway construction (Lv et al., 2012, 2014a, 2014b, 2020; Liu et al., 2014; Zhang et al., 2015; Zhou, 2017; Zhou et al., 2018b; Lv and Zhang, 2018; Wang and Chen, 2019; Cao et al., 2021; Li et al., 2021; Peng et al., 2021, 2022; Ding et al., 2023). Compared with the traditional circular pile, XCC piles can increase the side friction and give full play to the potential of pile material when the same amount of concrete material is used, thus improving the bearing capacity of the pile foundation. Until now, many works have been carried out to evaluate the influence of special X-shaped sections on the performances of XCC piles, mainly including model and field tests, numerical simulations, and theoretical analysis.

Lv et al. (2012, 2020) conducted a series of pile-foundation field tests, and found that XCC piles could provide superior vertical bearing characteristics to circular piles when the cross-section areas were equal. Subsequently, using the field-test data, Lv et al. (2014a, 2014b) and Lv and Zhang (2018) employed numerical

✉ Guangwei CAO, m_ma123@163.com
Guangwei CAO, https://orcid.org/0000-0001-7924-7732

Received July 31, 2023; Revision accepted Dec. 15, 2023;
Crosschecked June 8, 2024; Online first July 15, 2024

and theoretical methods to study the load-transfer mode of XCC piles under vertical load. The results showed that the geometric effect of the cross-section had a noteworthy influence on the pile tip resistance and the distribution of skin friction. Furthermore, they quantified the interaction between the XCC pile and soil under vertical load by a 3D analytical method which was proposed based on the principle of minimum potential energy and the variational method (Li et al., 2021). However, the impact of pile installation was not considered in the studies. Zhou et al. (2017) revealed the soil-deformation pattern during penetration of an XCC pile by performing transparent soil model tests. They then proposed a modified cavity-expansion model for predicting the radial displacement of soil during penetration (Liu et al., 2014; Zhou, 2017). Afterward, Zhou et al. (2019a) built a large deformation numerical model to investigate the 3D penetration mechanism during the installation of an XCC pile in undrained clay.

Regarding the bearing characteristics of XCC pile under lateral load, Zhou et al. (2018a, 2020a) established empirical models using the plane strain finite element limit method which could capture the ultimate lateral capabilities of XCC single and group piles in undrained clay. They proposed a simple hyperbolic *p*-*y* model (Zhou et al., 2020b) that took into consideration the elastic stiffness of the 2D laterally loaded XCC pile-soil system (Zhou et al., 2019b), where p is the lateral soil resistance per unit length and y is the lateral displacement of the pile. However, this model could not elucidate the 3D mechanism of laterally loaded XCC pile-soil interaction. Therefore, Zhou et al. (2022a) established a new *p*-*y* model to uncover the 3D failure mechanism of the soil around the XCC pile based on a series of well-calibrated 3D finite element analyses. Afterward, Zhou et al. (2022b) introduced this *p*-*y* model into the Winkler foundation model and proposed a simplified analysis model for predicting the lateral response of existing XCC piles induced by the penetration of adjacent piles under the undrained conditions.

Although numerous studies have been conducted on XCC piles, those described above were all conducted in clay soils. There were few reports on the investigation related to the XCC pile in sand. In addition, the previous studies mainly analyzed the deformation and stress development of the free-field soil in the XCC pile-penetration problem. However, in the actual engineering construction, there were existing piles in the vicinity of the penetrating pile. The compaction displacement load caused by the penetrating pile imposed additional bending moment on the existing pile, which would lead to damage or failure of the pile foundation. The purpose of this paper was to investigate the effect of the adjacent XCC pile penetration on the existing XCC pile in sand by means of a series of small-scale 1*g* model tests. The lateral response of an existing pile and the development of soil radial stress around the pile during penetration were analyzed by considering factors such as the relative density of the soil and the cross-section geometry of the existing pile.

2 Experimental equipment and materials

2.1 Test equipment

As shown in Fig. 1, the testing device included a movable sand pourer frame, loading device, square chamber, and data collection system. The movable sand pourer frame was mainly composed of iron brackets, a slide rail, and a chain block, whose construction and function are detailed below. During preparation of the sand foundation, the sand pourer device could move freely in six directions to control the homogeneity and relative density of the foundation. The loading equipment included a pile-penetration device and a control collection box. The servo control system for the equipment allowed for the implementation of various loading modes, which could be controlled either by displacement or force. The loading was controlled by displacement in this paper.

The chamber was assembled with transparent acrylic plates, angle steels, and bolts. To facilitate the arrangement of sensors and preparation of the sand foundation, the chamber was divided into two layers. The chamber had a width of 1000 mm and a height of 1050 mm. The distance between the chamber and the side of the existing pile was greater than $7D_{eq}$ (D_{eq}, defined as the equivalent diameter of XCC pile), and the bottom of the existing pile was located $4D_{eq}$ higher from the bottom of the chamber. Therefore, the distance between the model pile and the chamber sides in this study was large enough to eliminate the influence of the boundary effect according to the previous investigations (Gui et al., 1998; Bolton et al., 1999; Dong et al., 2018). During the test, a DH5921 high-frequency

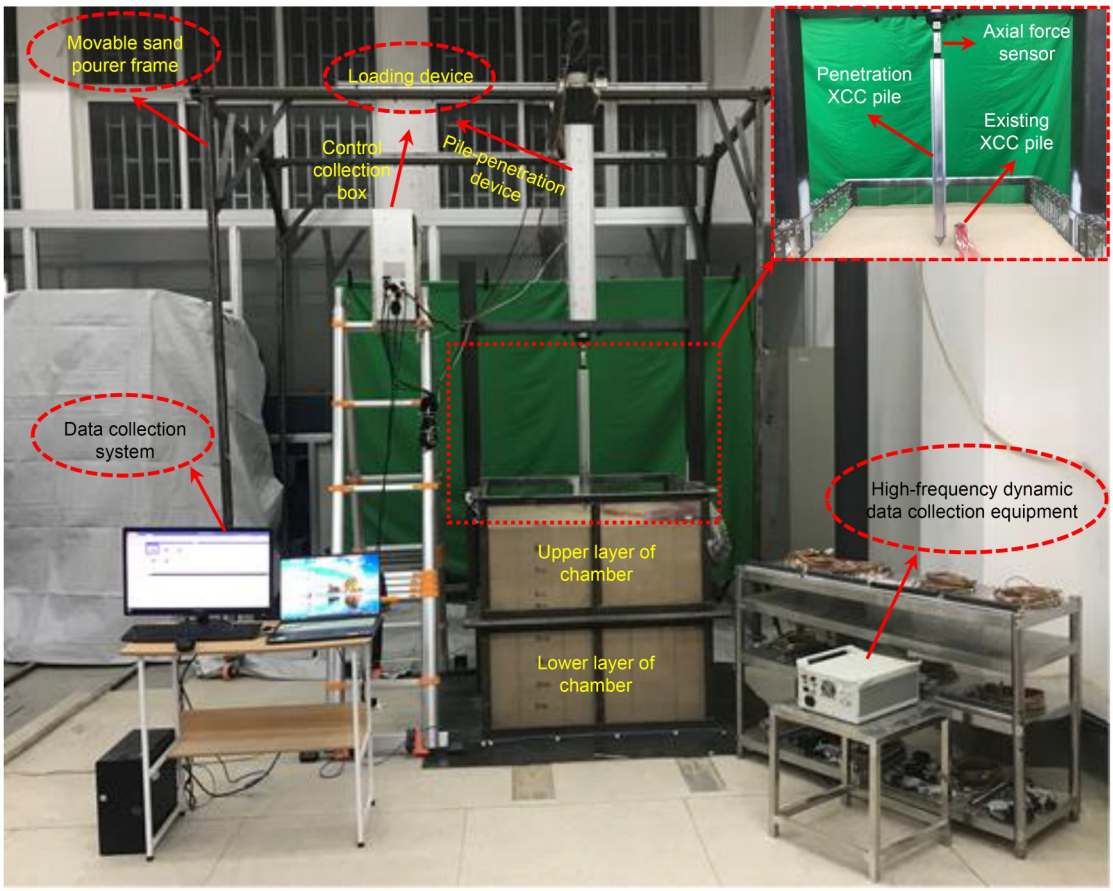

Fig. 1 Schematic view of the test device

dynamic acquisition system was employed to collect the strain data of the existing model pile and the soil pressure sensor data around the pile. The sampling frequencies of the strain gauge and soil pressure sensor are 100 Hz. The bending moment of the existing pile and the radial stress of the soil around the pile can be precisely acquired after the calibration of collected data.

2.2 Characteristics of sand

The sand used in this experimental study was Fujian standard sand. Table 1 gives the physical properties of the sand. The specific gravity was determined according to ASTM D854 (ASTM, 2016a), and the maximum and minimum dry densities were determined using the methods of ASTM D4253 (ASTM, 2016b) and D4254 (ASTM, 2016c). The particle size distribution curve of the sand is shown in Fig. 2. It should be mentioned here that all tests were conducted in dry sand because sandy soil is typically fully drained during penetration, due to its high permeability (Zhou et al., 2024).

Table 1 Physical properties of the test sand

Parameter	Value
Mean particle size, d_{50} (mm)	0.776
Coefficient of uniformity, C_u	1.41
Specific gravity, G_s	2.652
Maximum dry density, ρ_{dmax} (g/cm^3)	1.691
Minimum dry density, ρ_{dmin} (g/cm^3)	1.422

The model foundations of different relative densities in this test were prepared using the movable sand pourer frame and the sand pourer device by controlling the drop distance, as shown in Fig. 3a. Because the relative densities of the sand foundations were strongly affected by the drop distance as calibrated previously (Fig. 3b). Additionally, to ensure the uniformity of the model foundations, the sand was poured layer by layer.

2.3 Model piles

Fig. 4a shows the cross-section of the XCC pile, which consisted of four cambered and flat sections. The parameters a, b, and θ_x were employed to control the

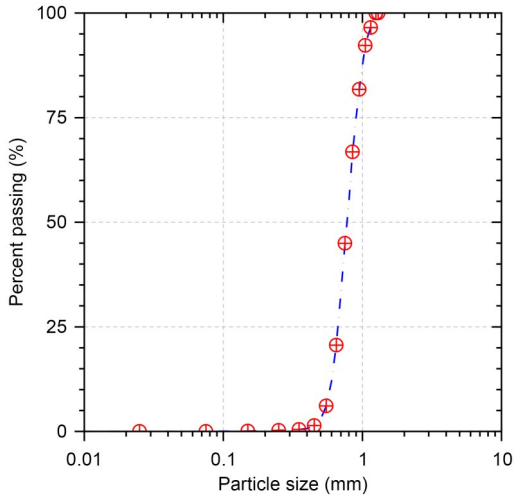

Fig. 2 Particle size distribution curve of the test sand

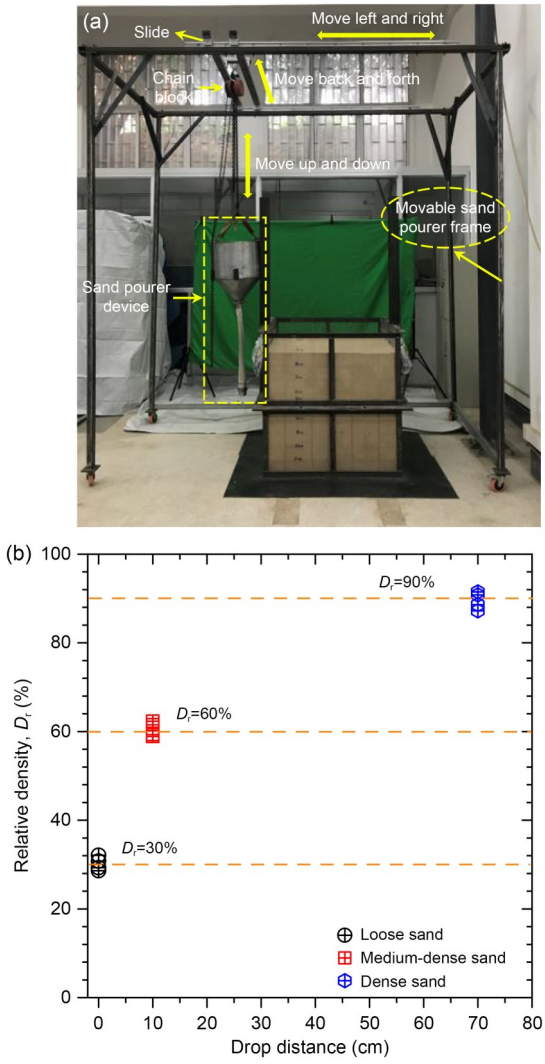

Fig. 3 (a) Model foundation preparation device; (b) Calibrated relationship between drop distance and relative density

geometric size and shape of the cross-section of the XCC pile. In engineering, θ_x is generally 90°, which is adopted in this study as well.

The existing model pile in this test had a length of 800 mm, and 700 mm of it had penetrated into the soil. The model pile was made of an aluminum alloy solid tube (type: 6061T6), which exhibited an elastic modulus of 68.9 GPa, Poisson's ratio of 0.33, tension yield strength of 275 MPa, and tensile strength of 305 MPa. It should be explained here that a real existing pile would generally be solid (with an elastic modulus of 30 GPa) and would be cast with the concrete material in actual engineering, but it was difficult to strictly control the material properties and cross-section geometry of the model concrete pile due to the limitations on its size. Therefore, the existing model piles were made of hollow aluminum alloy according to the principle of equal flexural stiffness without affecting the purpose of the experimental study. In addition, the pile end was sealed with an aluminum block during the test. Fig. 4b illustrates the cross-section of the existing model pile. Three existing XCC model piles of different geometries were designed, and their geometric dimensions and physical appearance are shown in Table 2 and Fig. 4c, respectively. The ratio b_1/a_1 varied from 0.1 to 0.5, which covered the range of the cross-section sizes of the XCC piles typically used in practical engineering. The penetrating XCC model pile (XCCPP in Table 2) was made as a rigid body, since the deformation of the pile body during penetration was very small. The angle of pile tip and penetration depth were 60° and 700 mm, respectively.

3 Experimental scheme

3.1 Test matrix

Taking the relative densities of soil (D_r) and the geometries of the cross-section (b_1/a_1) as the variables, we performed six sets of small-scale 1*g* model tests to investigate the lateral responses of the existing pile and the development of soil stress around the pile during the penetration of an adjacent XCC pile in sand. Table 3 shows the test program, in which T1–T3 investigated the influence of D_r and T4–T6 investigated the influence of b_1/a_1. The cross-section geometry and relative density were the same for T2 and T5, which could be used to evaluate the reliability of the tests. The distance

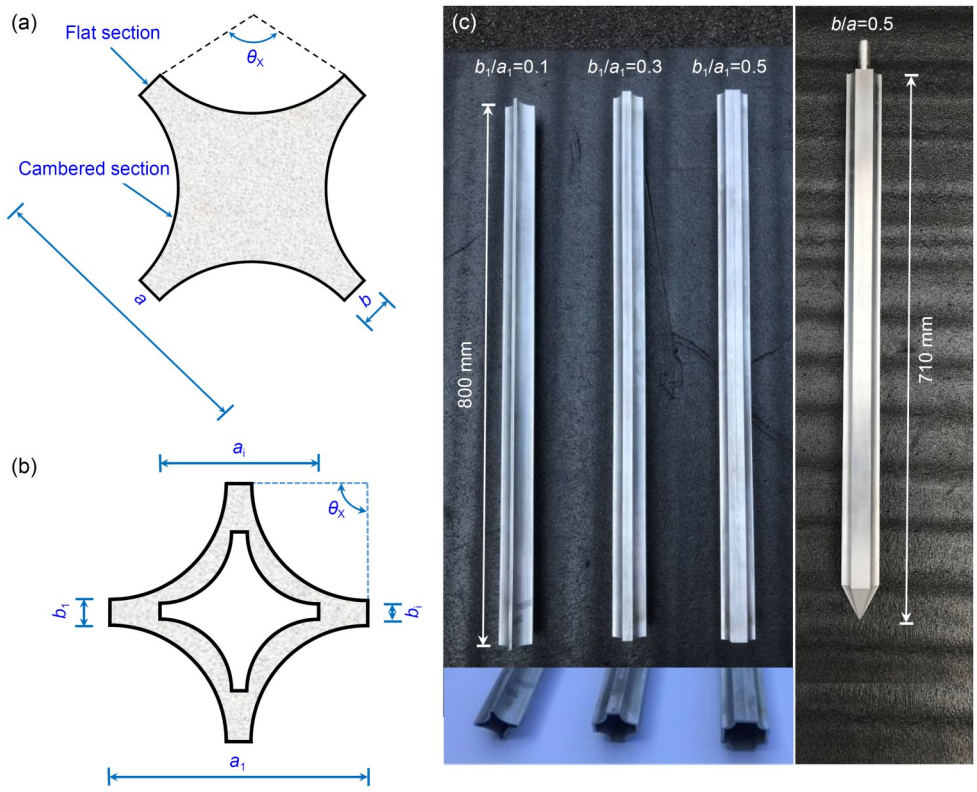

Fig. 4 Model test piles: (a) XCC pile cross-section; (b) existing XCC model pile cross-section; (c) existing model piles and adjacent model pile. a_1 and b_1 represent the outer dimensions of the model pile, and a_i and b_i represent the inner dimensions

Table 2 Geometrical dimension parameters of existing model piles

Pile number	b_1/a_1	b_1 (mm)	a_1 (mm)	b_i (mm)	a_i (mm)
XCCEP1	0.1	5	50	4.33	43.34
XCCEP2	0.3	15	50	13.00	43.34
XCCEP3	0.5	25	50	21.67	43.34
XCCPP	b/a=0.5, a=50 mm				

Table 3 Test program

Influence factor	Test number	D_r	b_1/a_1
Relative density	T1	30%	0.3
	T2	60%	0.3
	T3	90%	0.3
Cross-section geometry	T4	60%	0.1
	T5	60%	0.3
	T6	60%	0.5

between the axes of the penetrating pile and the existing pile was set to 80 mm (i.e., $1.6a_1$). In the test, the impact of the head load of the existing pile was not taken into account and the boundary condition of the pile head was free.

3.2 Instrumentation

To measure the bending moment of the existing pile, we installed miniature high-precision strain gauges with a length of 3 mm and resistance of 120 Ω along the body of the existing model pile. Ten locations were selected at uniform intervals of 80 mm along the pile length starting from the pile end under the premise of satisfying the requirements for measuring the bending moment profile. Paired strain gauges were arranged symmetrically at each elevation. In addition, all strain gauges on the model pile were coated with epoxy to protect them and the wires from damage. Fig. 5 shows a schematic diagram of the strain gauge arrangement around the existing XCC model pile. We should mention here that the strain gauges of each existing model pile were calibrated using the method for a simple supported beam before conducting the test, and then the bending moment of the existing model pile during the penetration was back-calculated from the calibration coefficient.

We employed a micro silicon piezoresistive high-frequency dynamic soil pressure sensor with a measurement range of 0–500 kPa and precision of 0.2% to

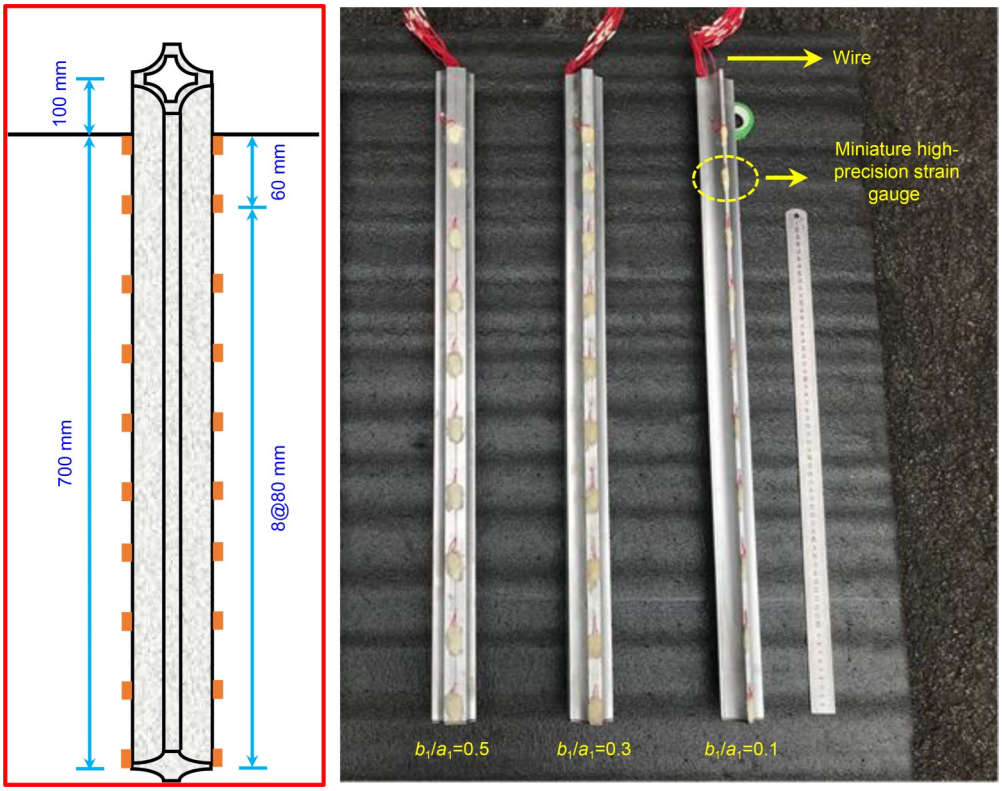

Fig. 5 Schematic diagram of the strain gauge layout for the existing model pile

study the stress change of soil during the penetration. According to the experimental scheme, three representative depths, i.e., vertical heights z/R (R=a_1/2) of 8, 16, and 24, were first selected. Then, for each depth, we installed miniature soil pressure sensors along the radial direction of the strong and weak axial profiles of the existing XCC pile to measure the soil radial stresses at radial distances r/R of 2, 4, and 8. Fig. 6 gives the elevation of the soil pressure sensor arrangement. The plan view of the sensors installed at different depths is shown in Fig. 7.

3.3 Test procedure

Before preparing the model foundation, we fixed the existing XCC model pile at the specified location using a T-shaped aluminum alloy square tube and a square hoop, as shown in Fig. 8. Note that the installation effect was neglected in this test, i.e., the "wish-in-place" method was adopted for installing the existing model pile. This is because Anusic et al. (2019) found that the installation method had a very limited impact on the characteristics of the laterally loaded pile, based on field experiments. Moreover, this approach prevented a change in the soil state around the pile arising from the installation of the existing pile and the buckling deformation of the existing pile itself. After the foundation was prepared using the sand pourer, the T-shaped construction was dismantled without disturbing the existing pile. The penetrating XCC pile was then installed on the pile-penetration device. Finally, the penetrating XCC pile was installed by the pile foundation penetration device at a speed of 1 mm/s (Gui et al., 1998; Bolton et al., 1999; Arshad et al., 2014). Meanwhile, the strain data of the existing pile and the soil pressure sensor data around the pile were collected using the data acquisition system.

4 Experimental results and discussion

4.1 Influence of relative density

4.1.1 Lateral response of the existing pile

Fig. 9 shows the bending moment (M) profiles of the existing XCC pile during the penetration of the adjacent XCC pile with relative densities D_r of 30%, 60%, and 90% when the penetration depth H was 100 mm, 200 mm, 300 mm, 400 mm, 500 mm, 600 mm,

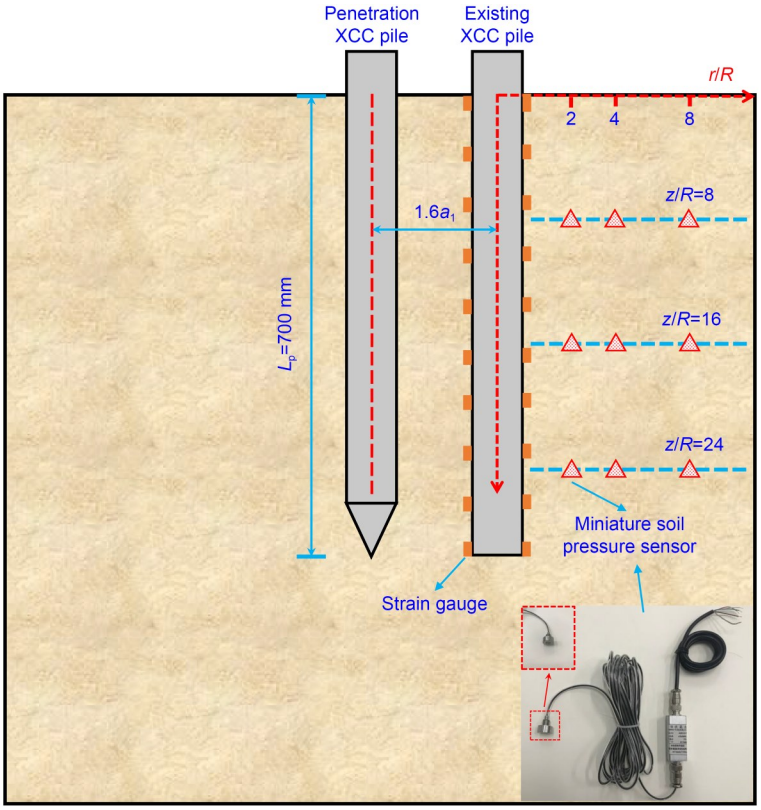

Fig. 6 Elevation of soil pressure sensor arrangement. L_p is the embedded length of existing model pile

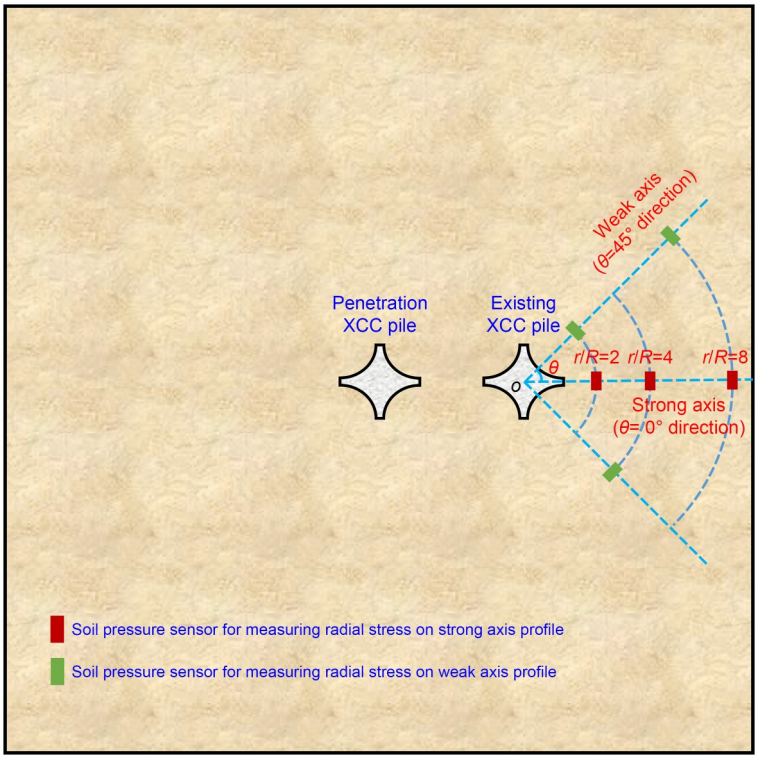

Fig. 7 Plan view of soil pressure sensor installation at various measurement depths. θ is the layout direction of soil pressure sensor

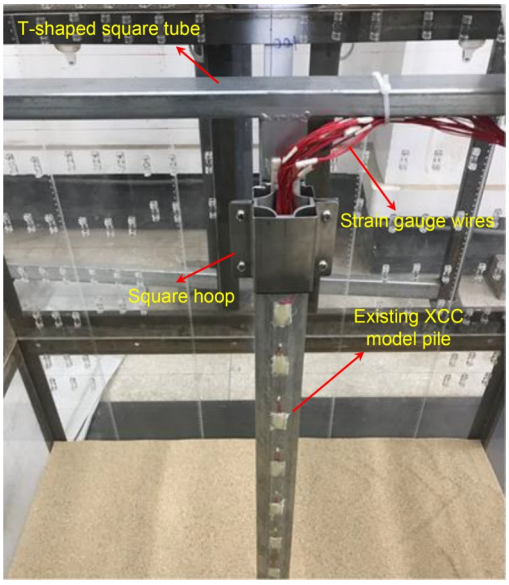

Fig. 8 Fixed existing model pile device

and 700 mm. It should be noted here that the positive bending moments involved in the following analysis indicate that the existing pile bends away from the adjacent pile, while the negative bending moments indicate that the existing pile bent toward the adjacent pile. In addition, the location of the measured maximum bending moment should not necessarily be consistent with that of the actual maximum bending moment since the distance between the adjacent strain gauges along the pile length was 80 mm, but it should be close.

As can be observed from the figure, the corresponding profiles at the same penetration depth varied significantly with D_r, but the shapes of the bending moment profiles were similar. For shallow penetration depths (H=100 mm and 200 mm), the bending profile exhibited a negative bending moment, indicating that the existing pile bent toward the penetration one. Moreover, the negative bending moment increased with increasing values of H, but the elevation of the maximum bending moment gradually moved down; for example, the maximum bending moments occurred at 380 mm and 460 mm below the surface when H was 100 mm and 200 mm, respectively. This is because the shallow soil movement and lateral soil pressure induced by penetration of the adjacent pile were concentrated in the upper section of the existing pile, which made the top part of the existing pile move away from the adjacent penetration pile. Meanwhile, the middle part of the existing pile rebounded to a certain extent, resulting in it bending towards the adjacent penetration pile.

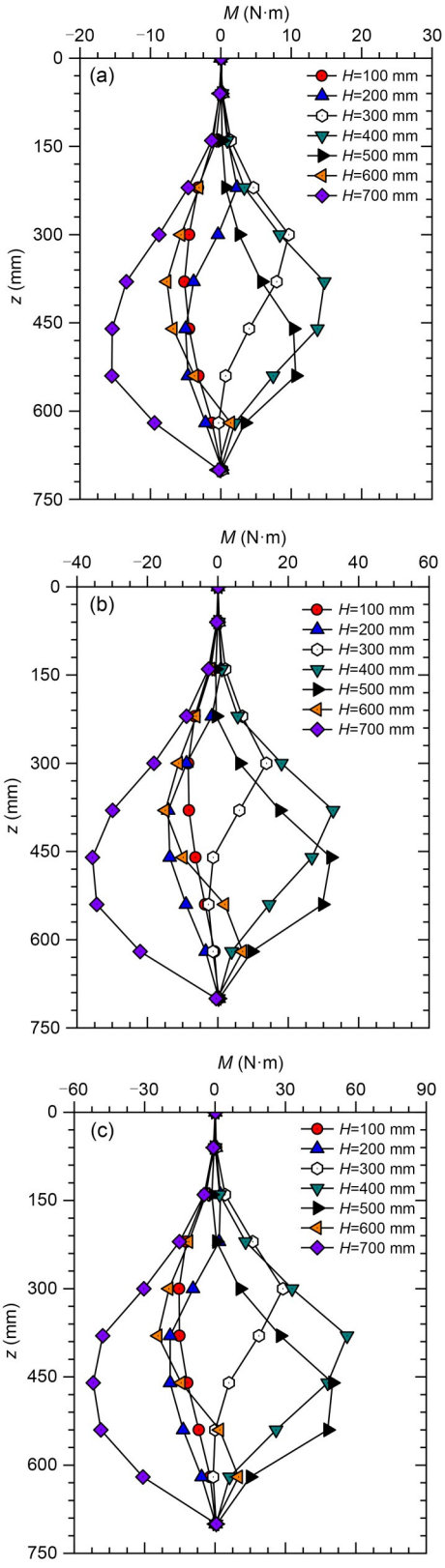

Fig. 9 Bending moment (M) profiles of the existing pile during penetration of the adjacent pile: (a) D_r=30%; (b) D_r=60%; (c) D_r=90%

As the adjacent XCC pile penetrated further (H= 300 mm, 400 mm, and 500 mm), the pile bending direction changed and its profile exhibited a positive bending moment. With the increase of H, the positive bending moment increased and then decreased, and the maximum bending moment occurred at the elevation close to the corresponding penetration depth. This was due to the fact that the soil movement extended deeper with increasing penetration depth, causing the soil movement within a certain depth below the surface to be very intense. The soil movement and lateral soil pressure were mainly concentrated in the middle of the pile, thus pushing the middle of the existing pile and making it bend away from the adjacent penetration pile. With deep penetration (H=600 mm and 700 mm), the existing pile again bent towards the adjacent pile, and its bending moment was negative. The position of the maximum bending moment did not occur near the corresponding penetration depth, but gradually moved down as H increased. This could be explained by the fact that at deeper penetration depths, the soil movement directed to the existing pile reached its maximum and was concentrated within the range of the pile end. As a result, the pile end deviated from the direction of the adjacent pile. As with shallow penetration, a corresponding rebound also occurred in the middle of the pile at this point, thus making the existing pile bend towards the adjacent penetration pile.

Fig. 10 compares the bending moments of the existing XCC pile caused by the penetration of adjacent piles in the sand of different relative densities. Four penetration depths H of $L_p/4$, $L_p/2$, $3L_p/4$, and L_p were

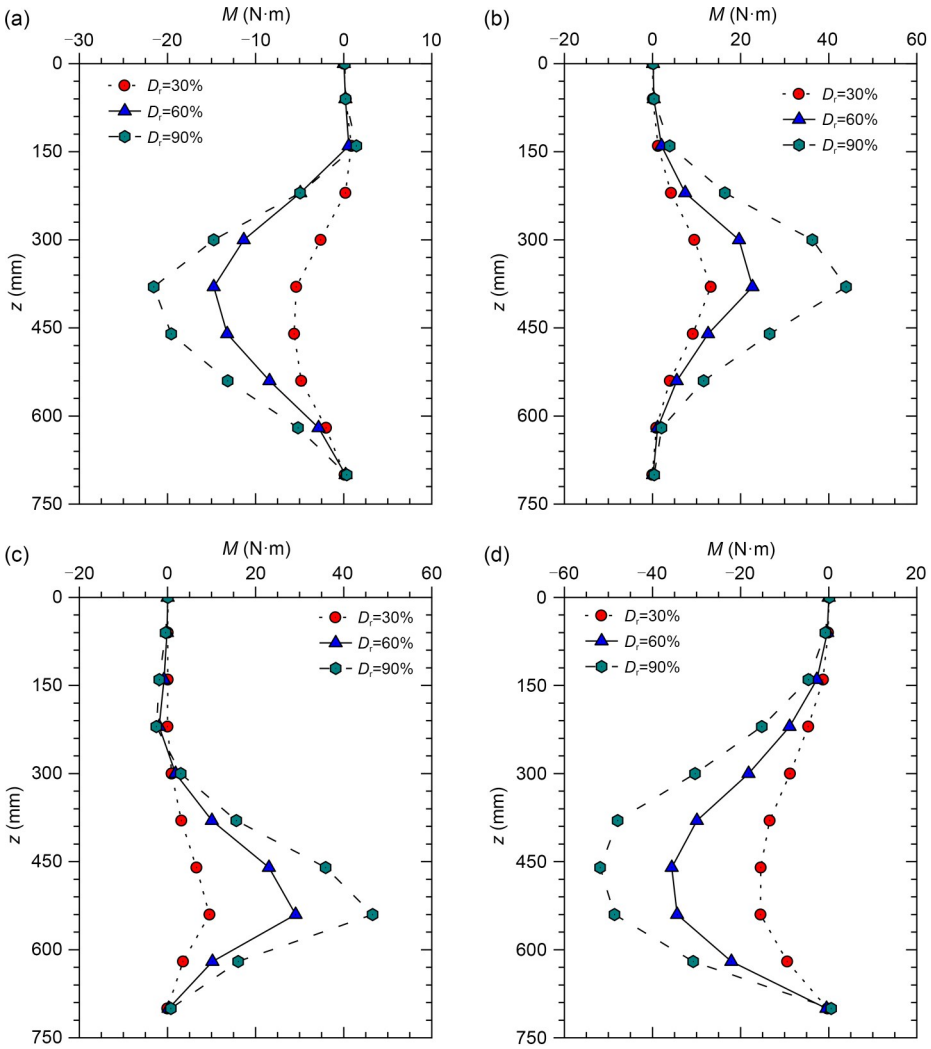

Fig. 10 Comparison of the bending moments of the existing pile during the penetration: (a) $H=L_p/4$; (b) $H=L_p/2$; (c) $H=3L_p/4$; (d) $H=L_p$

selected. It can be seen from the figure that the bending moment of the existing pile increased with the increase of D_r for any given H, and all the maximum bending moments almost occurred at the same elevation. The dilatancy behavior became more significant and the peak friction angle also increased with the gradual compaction of soil during the shearing process, thus increasing the soil resistance around the existing pile. The bending moment of the existing pile corresponding to each relative density reached its maximum value at a penetration depth of L_p. The maximum bending moment in dense sand (D_r=90%) was −51.89 N·m, while it was −15.49 N·m in loose sand (D_r=30%), which was only 29.85% of that in dense sand.

4.1.2 Development of soil stress around the existing pile

Fig. 11 shows the variations of radial stress σ'_r (normalized by the initial vertical gravity stress σ'_{v0}) with the penetration depth H/R at r/R=2 of the strong and weak axis profiles of the existing XCC pile during the penetration of the adjacent XCC pile in sands of D_r=30%, 60%, and 90%. It can be seen from the figure that radial stress σ'_r/σ'_{v0} of soil around the existing XCC pile exhibited different development trends at different measured depths (z/R=8, 16, and 24). As H/R increased, the normalized radial stress σ'_r/σ'_{v0} at a measurement depth of z/R=8 below the surface first increased, then decreased, and finally became miniscule.

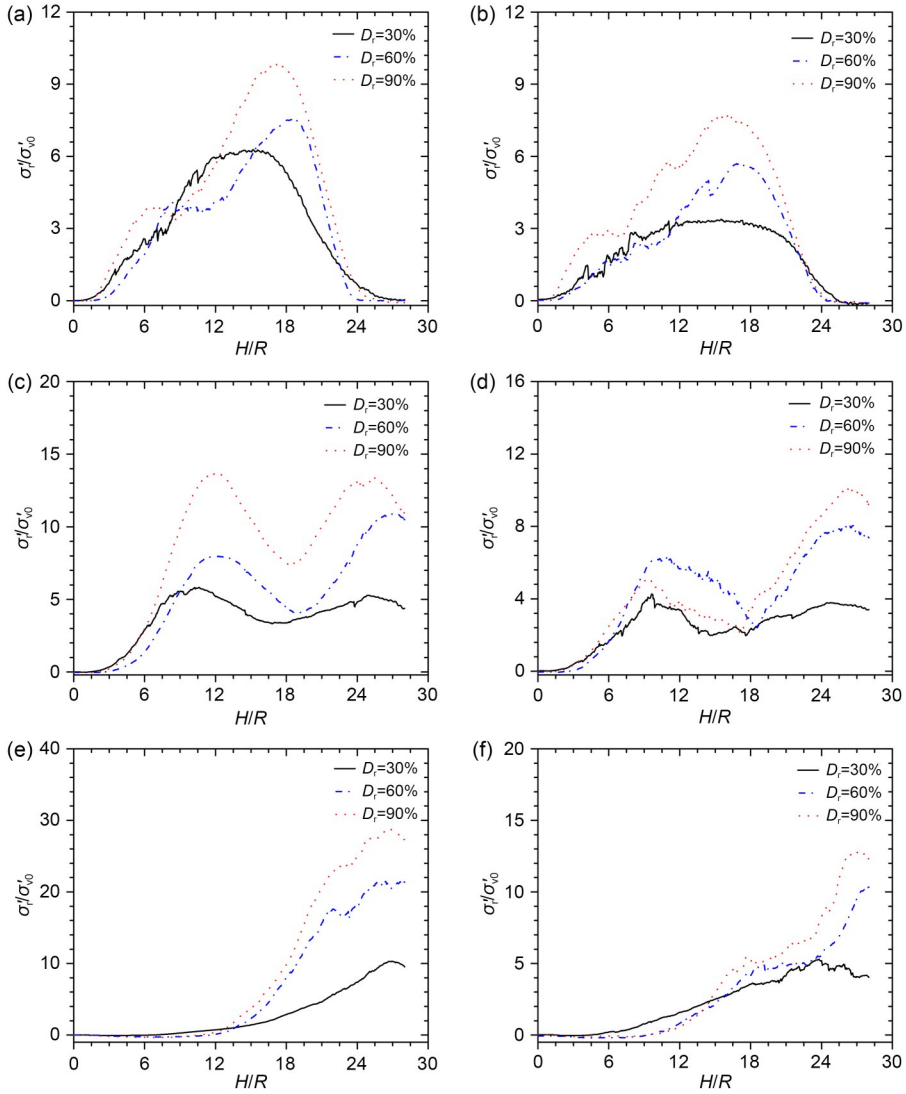

Fig. 11 Variation of σ'_r/σ'_{v0} with H/R at r/R=2 away from the pile axial during the adjacent XCC pile penetration: (a) z/R=8, strong axis profile; (b) z/R=8, weak axis profile; (c) z/R=16, strong axis profile; (d) z/R=16, weak axis profile; (e) z/R=24, strong axis profile; (f) z/R=24, weak axis profile

The σ'_r/σ'_{v0} value reached its peak at a penetration depth of H=17R and was close to zero at approximately H=24R. For the measured depth of z/R=16, the normalized radial stress showed an "M-shaped" variation trend with the increase of H/R. The locations of two peaks of σ'_r/σ'_{v0} occurred at penetration depths of H=11R and 26R. Compared with the variation pattern of soil radial stress at z/R=8, the stress reduction in the range of H=11R–19R could be attributed to the change in the bending pattern of the existing pile during the transition from shallow to middle penetration, which is evident from Fig. 9. At a depth of z/R=24, the value of σ'_r/σ'_{v0} was almost zero before the adjacent XCC pile penetrated to a depth of 10R. Then, it increased to the peak value at H=26R followed by a decrease stage with the increasing penetration depth H/R. In addition, compared with the penetration of the pile in the free-field soil, the variations of the radial stress of soil did not exhibit the "h/R effect" due to the shielding effect of the existing XCC pile. The "h/R effect" means that the radial stress of the soil around the pile body decreased with the increase of the relative depth from the pile tip, where h was defined as the relative height above the pile tip or the relative height below the pile tip (Jardine et al., 2013a, 2013b; Yang et al., 2014, 2020).

Fig. 12 illustrates the variations of the normalized peak radial stress $\sigma'_{r\_max}/\sigma'_{v0}$ of soil around the existing

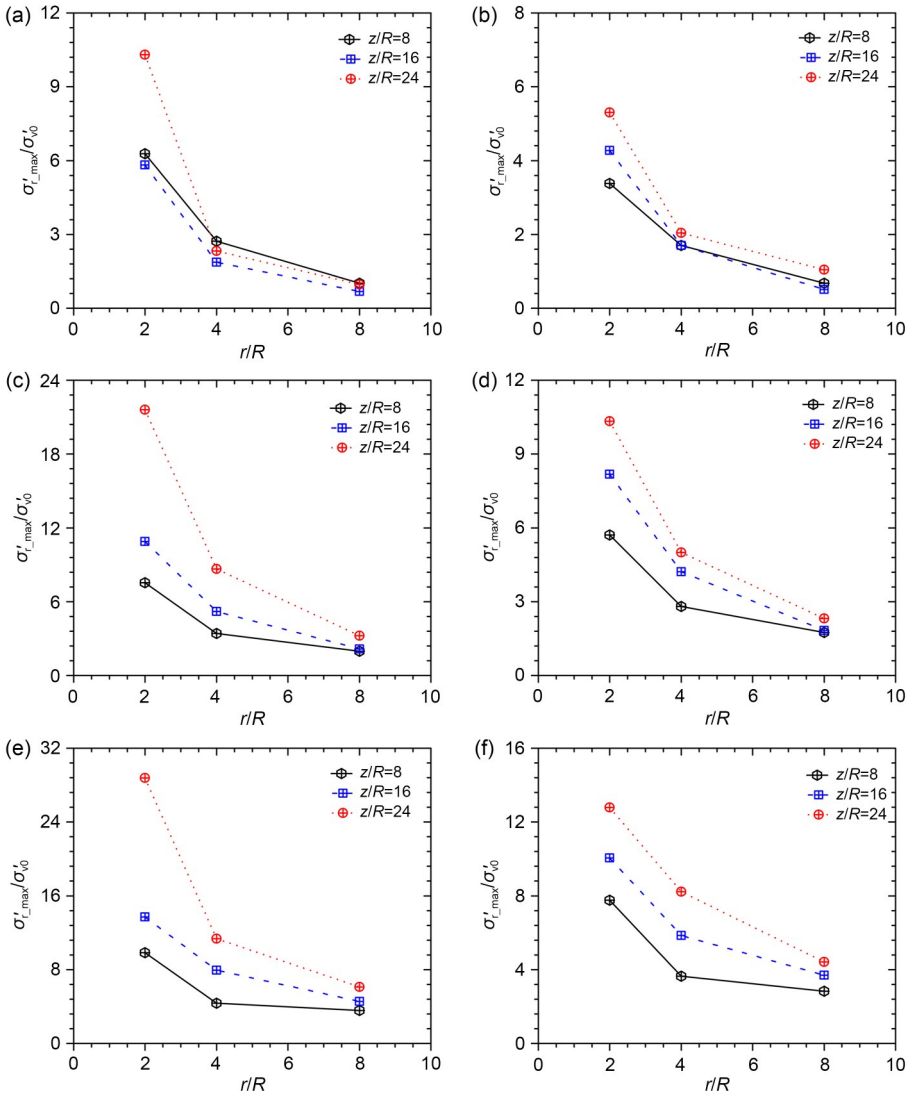

Fig. 12 Relationship between $\sigma'_{r\_max}/\sigma'_{v0}$ and r/R during the penetration: (a) D_r=30%, strong axis profile; (b) D_r=30%, weak axis profile; (c) D_r=60%, strong axis profile; (d) D_r=60%, weak axis profile; (e) D_r=90%, strong axis profile; (f) D_r=90%, weak axis profile

XCC pile with the radial distance r/R from the pile axis during the penetration in sand of different relative densities. One can see that the normalized peak radial stress $\sigma'_{r\_max}/\sigma'_{v0}$ decreased exponentially as r/R increased, and the decay rates of $\sigma'_{r\_max}/\sigma'_{v0}$ from r/R=2 to 4 were much larger than those from 4 to 8. Moreover, the gap between the $\sigma'_{r\_max}/\sigma'_{v0}$ at each measurement depth gradually narrowed with increasing r/R. Compared with the medium-dense and dense sands (D_r=60% and 90%), the attenuation index of $\sigma'_{r\_max}/\sigma'_{v0}$ along the radial direction in loose sand (D_r=30%) was greater.

4.2 Influence of cross-section geometry

4.2.1 Lateral response of existing pile

Fig. 13 shows the effect of the cross-section geometry on the bending moment of the existing XCC pile at four typical penetration depths (H=L_p/4, L_p/2, 3L_p/4, and L_p). It is clear that as the cross-section geometry parameter b_1/a_1 increased, the bending moment of the existing pile increased, and that all the maximum bending moments occurred at the same location in the pile. This is because the cross-section geometry affected the distribution of soil resistance inside the

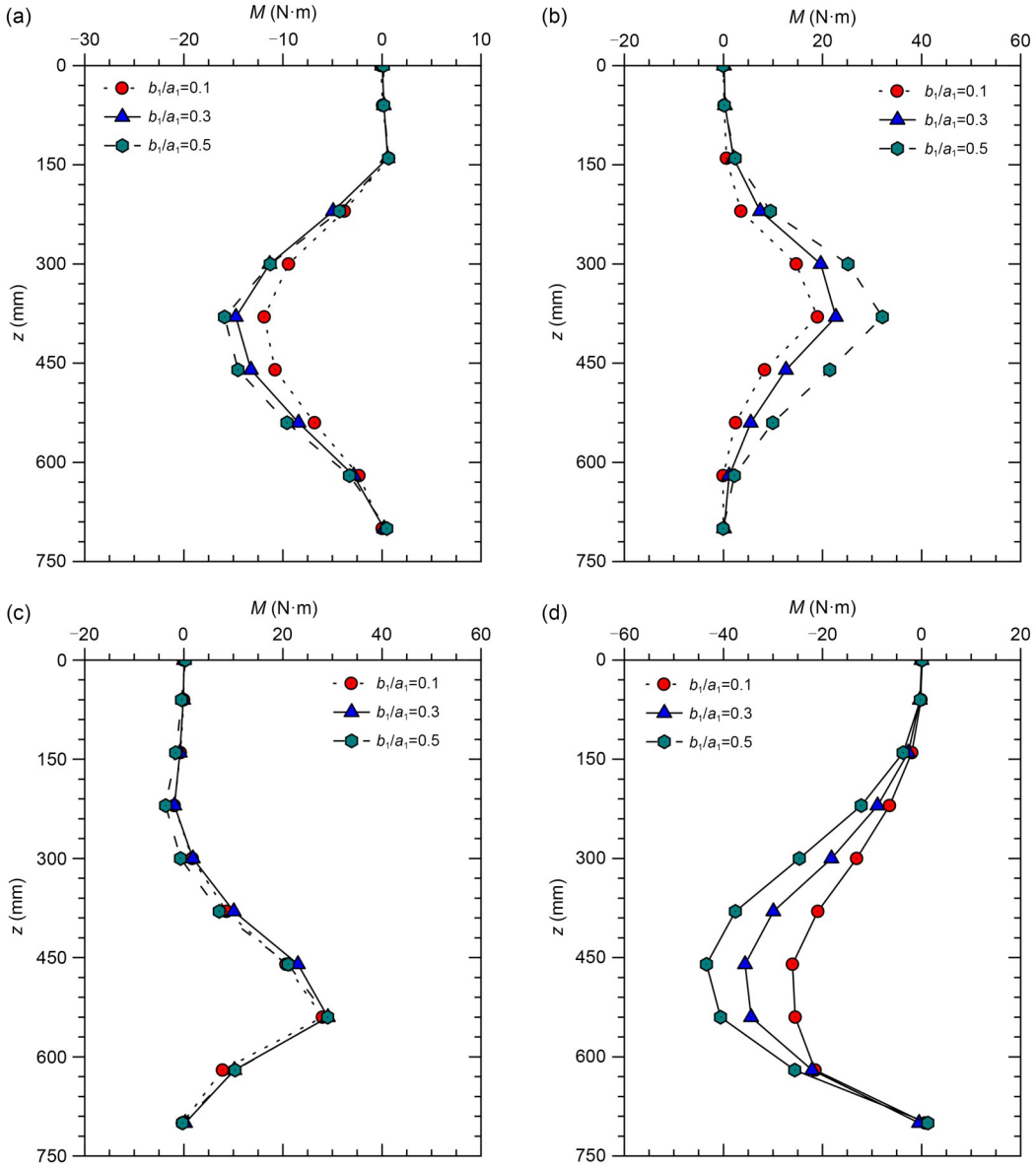

Fig. 13 Comparison of the bending moments of existing piles with b_1/a_1=0.1, 0.3, and 0.5 during the adjacent XCC pile penetration: (a) H=L_p/4; (b) H=L_p/2; (c) H=3L_p/4; (d) H=L_p

pile, resulting in a complex nonlinear pile-soil interaction. Furthermore, the maximum bending moments corresponding to b_1/a_1=0.1, 0.3, and 0.5 were −26.06 N·m, −35.60 N·m, and −43.42 N·m at a penetration depth of L_p, respectively, which increased by 36.60% and 22.00%. This indicates that cross-section geometry had a significant effect on the lateral response of the existing XCC pile. Specifically, the existing XCC pile had a stronger ability to resist the lateral load as b_1/a_1 decreased.

4.2.2 Development of soil stress around the existing pile

Fig. 14 presents the variations of the normalized radial stress σ'_r/σ'_{v0} with the penetration depth H/R at r/R=2 of the strong and weak axis profiles of the existing XCC piles with b_1/a_1=0.1, 0.3, and 0.5 during the penetration. For a given cross-section geometry parameter b_1/a_1, the relationship between σ'_r/σ'_{v0} and H/R showed different variation patterns at different measurement depths (z/R=8, 16, and 24). These trends were similar to those in Fig. 11, so we will not describe them again here. Fig. 15 gives the variations of the normalized peak radial stress $\sigma'_{r\_max}/\sigma'_{v0}$ with the radial distance r/R for b_1/a_1=0.1, 0.3, and 0.5 during the penetration. It can be seen from the figure that $\sigma'_{r\_max}/\sigma'_{v0}$ decreased exponentially with the increase of r/R as well. Furthermore, at the same soil location, $\sigma'_{r\_max}/\sigma'_{v0}$ increased with increasing b_1/a_1.

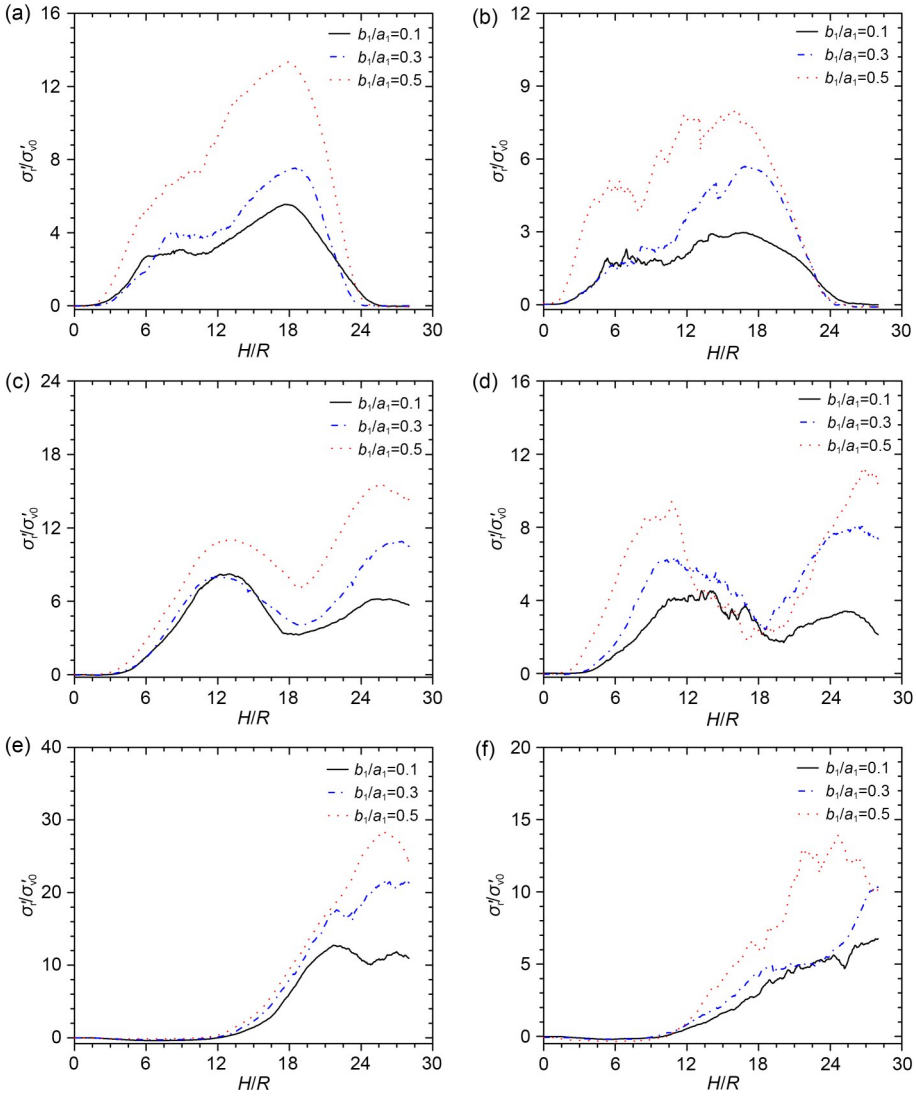

Fig. 14 Variation of σ'_r/σ'_{v0} with H/R at r/R=2 during the adjacent XCC pile penetration: (a) z/R=8, strong axis profile; (b) z/R=8, weak axis profile; (c) z/R=16, strong axis profile; (d) z/R=16, weak axis profile; (e) z/R=24, strong axis profile; (f) z/R=24, weak axis profile

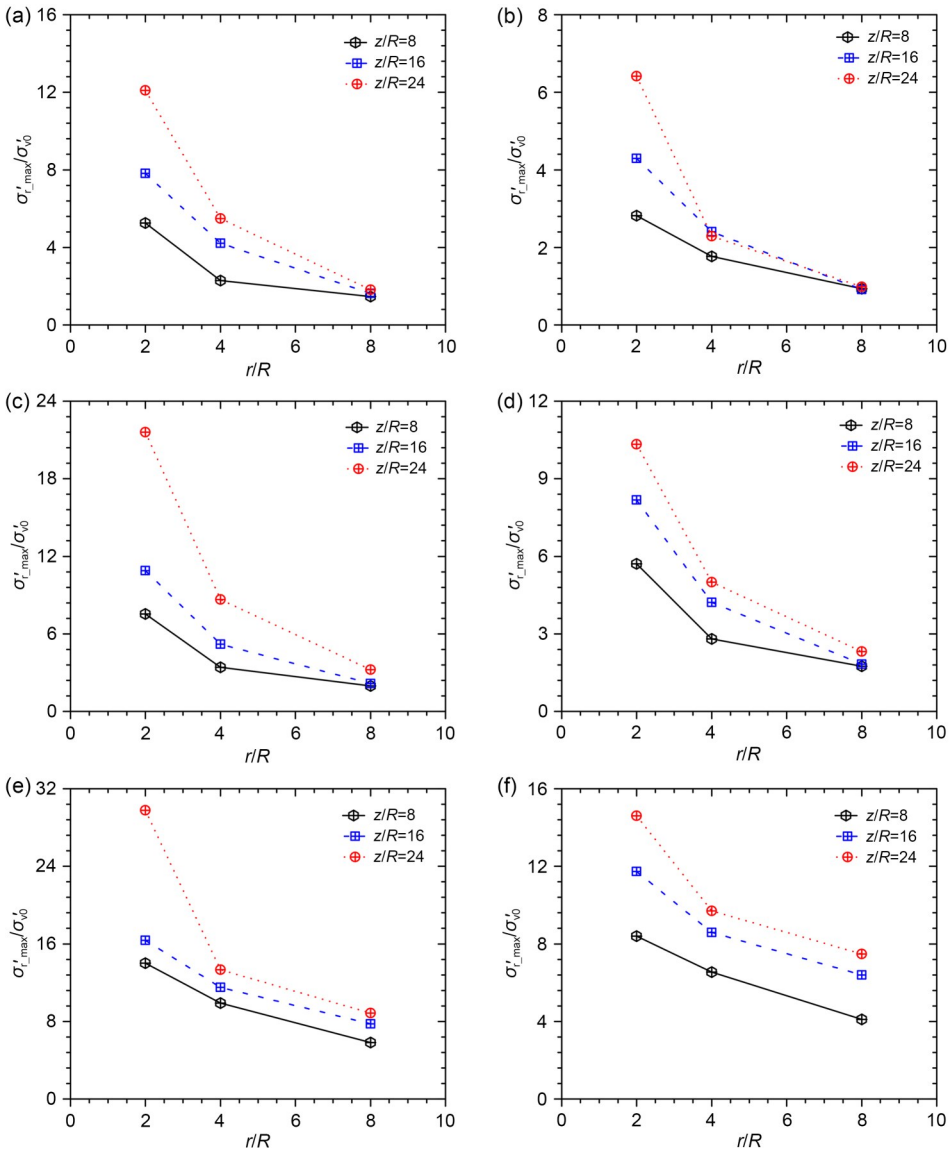

Fig. 15 Relationship between $\sigma'_{r\_max}/\sigma'_{v0}$ and r/R during the penetration: (a) b_1/a_1=0.1, strong axis profile; (b) b_1/a_1=0.1, weak axis profile; (c) b_1/a_1=0.3, strong axis profile; (d) b_1/a_1=0.3, weak axis profile; (e) b_1/a_1=0.5, strong axis profile; (f) b_1/a_1=0.5, weak axis profile

5 Conclusions

A series of small-scale 1*g* model tests were performed in this paper to study the effect of the penetration of an adjacent XCC pile on existing XCC piles in sand. Taking into account the relative density of soil and the cross-section geometry of the existing pile, we analyzed the lateral response of the existing pile and soil stress development during the penetration. Based on the observed results, we obtained the following conclusions:

1. The existing XCC pile exhibits different bending patterns during the penetration of an adjacent XCC pile. With shallow penetration, the existing pile bends toward the adjacent XCC pile. The bending moment increases along with *H*, but the position of the maximum bending moment gradually moves downward. With mid-level penetration, the bending moment first increases and then decreases with the value of *H*, and the maximum bending moment occurs near the corresponding penetration depth. With deep penetration, the existing pile again bends towards the adjacent XCC pile.

The location of the maximum bending moment gradually moved down from the upper part with increasing H.

2. The relative density (D_r) and cross-section geometry (b_1/a_1) have significant effects on the lateral response of the existing pile. The bending moment increases with increasing D_r and b_1/a_1 for a given H. The maximum bending moment of the existing pile in loose sand (D_r=30%) is only 29.85% of that in dense sand (D_r=90%). It increases by 36.60% and 22.00% when the cross-section geometry parameter b_1/a_1 increases from 0.1 to 0.3 and from 0.3 to 0.5, respectively. This means that the smaller the b_1/a_1, the higher the capacity to resist lateral load.

3. The variations of the radial stress of soil around the existing pile with the penetration depth at various measurement depths show different patterns during the penetration. In addition, compared with penetration in free-field soil, the variations of the radial stress do not show the "h/R effect" because of the shading effect of the existing XCC pile.

4. The peak of radial stress $\sigma'_{r\_max}/\sigma'_{v0}$ decreases exponentially with increasing radial distance r/R. The decay index of $\sigma'_{r\_max}/\sigma'_{v0}$ with r/R in loose sand (D_r= 30%) is larger than those in medium-dense and dense sands (D_r=60% and 90%). The peak of radial stress at the same soil location exhibits an increasing trend with the increase of b_1/a_1.

There are some limitations that must be addressed for the work done in this study. The soil arching effect caused by the pre-buried soil pressure sensor causes measurement error, which needs to be considered in future model tests. In addition, due to the limitations of the small-scale 1g model test, we could only qualitatively analyze the lateral response of the existing pile and the development of soil radial stress around the pile during the penetration, and it was difficult to obtain a quantitative relationship. In follow-up work, we plan to adopt the discrete element method to establish a full-scale model for quantitative research.

Acknowledgments

This work is supported by the National Natural Science Foundation of China (Nos. 52308352, 52238009, and 52108321), the Jiangxi Provincial Natural Science Foundation of China (No. 20232BAB214082), the Open Research Fund Program of Guangdong Key Laboratory of Earthquake Engineering and Application Technology (No. 2020B1212060071), and the Science & Technology Project of the Education Department of Jiangxi Province (No. GJJ2200681), China.

Author contributions

Peng ZHOU designed the research and wrote the first draft of the manuscript. Jianhui XU and Guangwei CAO processed the corresponding data. Xuanming DING helped to organize the manuscript. Changjie XU and Jie CUI revised and edited the final version.

Conflict of interest

Peng ZHOU, Jianhui XU, Changjie XU, Guangwei CAO, Jie CUI, and Xuanming DING declare that they have no conflict of interest.

References

Anusic I, Lehane BM, Eiksund GR, et al., 2019. Influence of installation method on static lateral response of displacement piles in sand. *Géotechnique Letters*, 9(3):193-197. https://doi.org/10.1680/jgele.18.00191

Arshad MI, Tehrani FS, Prezzi M, et al., 2014. Experimental study of cone penetration in silica sand using digital image correlation. *Géotechnique*, 64(7):551-569. https://doi.org/10.1680/geot.13.P.179

ASTM (American Society for Testing and Materials), 2016a. Standard Test Methods for Specific Gravity of Soil Solids by Water Pycnometer, ASTM D854. ASTM.

ASTM (American Society for Testing and Materials), 2016b. Standard Test Methods for Maximum Index Density and Unit Weight of Soils Using a Vibratory Table, ASTM D4253-16. ASTM.

ASTM (American Society for Testing and Materials), 2016c. Standard Test Methods for Minimum Index Density and Unit Weight of Soils and Calculation of Relative Density, ASTM D4254-16. ASTM.

Bolton MD, Gui MW, Garnier J, et al., 1999. Centrifuge cone penetration tests in sand. *Géotechnique*, 49(4):543-552. https://doi.org/10.1680/geot.1999.49.4.543

Cao GW, Chen ZX, Wang CL, et al., 2020. Dynamic responses of offshore wind turbine considering soil nonlinearity and wind-wave load combinations. *Ocean Engineering*, 217: 108155. https://doi.org/10.1016/j.oceaneng.2020.108155

Cao GW, Ding XM, Yin ZY, et al., 2021. A new soil reaction model for large-diameter monopiles in clay. *Computers and Geotechnics*, 137:104311. https://doi.org/10.1016/j.compgeo.2021.104311

Ding XM, Chian SC, Lian J, et al., 2023. Wind-wave combined effect on dynamic response of soil-monopile-OWT system considering cyclic hydro-mechanical clay behavior. *Computers and Geotechnics*, 154:105124. https://doi.org/10.1016/j.compgeo.2022.105124

Dong JM, Chen F, Zhou M, et al., 2018. Numerical analysis of the boundary effect in model tests for single pile under lateral load. *Bulletin of Engineering Geology and the Environment*, 77(3):1057-1068. https://doi.org/10.1007/s10064-017-1182-5

Gui MW, Bolton MD, Garnier J, et al., 1998. Guidelines for cone penetration tests in sand. International Conference on Centrifuge 98, p.155-160.

Jardine RJ, Zhu BT, Foray P, et al., 2013a. Measurement of stresses around closed-ended displacement piles in sand. *Géotechnique*, 63(1):1-17. https://doi.org/10.1680/geot.9.P.137

Jardine RJ, Zhu BT, Foray P, et al., 2013b. Interpretation of stress measurements made around closed-ended displacement piles in sand. *Géotechnique*, 63(8):613-627. https://doi.org/10.1680/geot.9.P.138

Li XC, Zhou H, Liu HL, et al., 2021. Three-dimensional analytical continuum model for axially loaded noncircular piles in multilayered elastic soil. *International Journal for Numerical and Analytical Methods in Geomechanics*, 45(18): 2654-2681. https://doi.org/10.1002/nag.3281

Liu HL, Zhou H, Kong GQ, 2014. XCC pile installation effect in soft soil ground: a simplified analytical model. *Computers and Geotechnics*, 62:268-282. https://doi.org/10.1016/j.compgeo.2014.07.007

Lv YR, Zhang DD, 2018. Geometrical effects on the load transfer mechanism of pile groups: three-dimensional numerical analysis. *Canadian Geotechnical Journal*, 55(5): 749-757. https://doi.org/10.1139/cgj-2016-0518

Lv YR, Liu HL, Ding XM, et al., 2012. Field tests on bearing characteristics of X-section pile composite foundation. *Journal of Performance of Constructed Facilities*, 26(2): 180-189. https://doi.org/10.1061/(asce)cf.1943-5509.0000247

Lv YR, Liu HL, Ng CWW, et al., 2014a. A modified analytical solution of soil stress distribution for XCC pile foundations. *Acta Geotechnica*, 9(3):529-546. https://doi.org/10.1007/s11440-013-0280-1

Lv YR, Liu HL, Ng CWW, et al., 2014b. Three-dimensional numerical analysis of the stress transfer mechanism of XCC piled raft foundation. *Computers and Geotechnics*, 55: 365-377. https://doi.org/10.1016/j.compgeo.2013.09.019

Lv YR, Li X, Wang Y, 2020. Centrifuge and numerical modeling of geometrical effects on XCC piled rafts. *Soils and Foundations*, 60(6):1405-1421. https://doi.org/10.1016/j.sandf.2020.09.001

Peng Y, Liu HL, Li C, et al., 2021. The detailed particle breakage around the pile in coral sand. *Acta Geotechnica*, 16(6): 1971-1981. https://doi.org/10.1007/s11440-020-01089-2

Peng Y, Ding XM, Yin ZY, et al., 2022. Micromechanical analysis of the particle corner breakage effect on pile penetration resistance and formation of breakage zones in coral sand. *Ocean Engineering*, 259:111859. https://doi.org/10.1016/j.oceaneng.2022.111859

Wang HL, Chen RP, 2019. Estimating static and dynamic stresses in geosynthetic-reinforced pile-supported trackbed under train moving loads. *Journal of Geotechnical and Geoenvironmental Engineering*, 145(7):04019029. https://doi.org/10.1061/(asce)gt.1943-5606.0002056

Yang ZX, Jardine RJ, Zhu BT, et al., 2014. Stresses developed around displacement piles penetration in sand. *Journal of Geotechnical and Geoenvironmental Engineering*, 140(3): 04013027. https://doi.org/10.1061/(asce)gt.1943-5606.0001022

Yang ZX, Gao YY, Jardine RJ, et al., 2020. Large deformation finite-element simulation of displacement-pile installation experiments in sand. *Journal of Geotechnical and Geoenvironmental Engineering*, 146(6):04020044. https://doi.org/10.1061/(asce)gt.1943-5606.0002271

Zhang DD, Lv YR, Liu HL, et al., 2015. An analytical solution for load transfer mechanism of XCC pile foundations. *Computers and Geotechnics*, 67:223-228. https://doi.org/10.1016/j.compgeo.2015.03.006

Zhou H, 2017. Complex variable solution for boundary value problem with X-shaped cavity in plane elasticity and its application. *Applied Mathematics and Mechanics*, 38(9): 1329-1346. https://doi.org/10.1007/s10483-017-2235-8

Zhou H, Liu HL, Randolph MF, et al., 2017. Experimental and analytical study of X-section cast-in-place concrete pile installation effect. *International Journal of Physical Modelling in Geotechnics*, 17(2):103-121. https://doi.org/10.1680/jphmg.15.00037

Zhou H, Yuan JR, Liu HL, et al., 2018a. Analytical model for evaluating XCC pile shaft capacity in soft soil by incorporating penetration effects. *Soils and Foundations*, 58(5): 1093-1112. https://doi.org/10.1016/j.sandf.2018.04.005

Zhou H, Liu HL, Wang LH, et al., 2018b. Finite element limit analysis of ultimate lateral pressure of XCC pile in undrained clay. *Computers and Geotechnics*, 95:240-246. https://doi.org/10.1016/j.compgeo.2017.10.015

Zhou H, Yuan JR, Liu HL, 2019a. A general analytical solution for lateral soil response of non-circular cross-sectional pile segment. *Applied Mathematical Modelling*, 71:601-631. https://doi.org/10.1016/j.apm.2019.03.005

Zhou H, Liu HL, Yuan JR, et al., 2019b. Numerical simulation of XCC pile penetration in undrained clay. *Computers and Geotechnics*, 106:18-41. https://doi.org/10.1016/j.compgeo.2018.10.009

Zhou H, Liu HL, Li YZ, et al., 2020a. Limit lateral resistance of XCC pile group in undrained soil. *Acta Geotechnica*, 15(6):1673-1683. https://doi.org/10.1007/s11440-019-00855-1

Zhou H, Liu HL, Ding XM, et al., 2020b. A *p–y* curve model for laterally loaded XCC pile in soft clay. *Acta Geotechnica*, 15(11):3229-3242. https://doi.org/10.1007/s11440-020-00944-6

Zhou P, Liu HL, Zhou H, et al., 2022a. A lateral soil resistance model for XCC pile in soft clay considering the effect of the geometry of cross section. *Acta Geotechnica*, 17(10): 4681-4697. https://doi.org/10.1007/s11440-022-01510-y

Zhou P, Liu HL, Zhou H, et al., 2022b. A simplified analysis approach for the effect of the installation of adjacent XCC pile on the existing single XCC pile in undrained clay. *Acta Geotechnica*, 17(12):5499-5519. https://doi.org/10.1007/s11440-022-01543-3

Zhou P, Liu HL, Zhou H, et al., 2024. Experimental study on the development of surrounding soil stress during XCC pile installation in sand. *Acta Geotechnica*, 19:4017-4035. https://doi.org/10.1007/s11440-023-02147-1